Monthly Notices of the ROYAL ASTRONOMICAL SOCIETY

MNRAS **497,** 52–66 (2020) doi:10.1093/mnras/staa1766
Advance Access publication 2020 June 19

Shapley supercluster survey: mapping the dark matter distribution

Yuchi Higuchi [1,2]★ Nobuhiro Okabe [3,4,5] Paola Merluzzi,[6] Christopher Paul Haines,[7] Giovanni Busarello,[6] Aniello Grado[6] and Amata Mercurio[6]

[1]*National Astronomical Observatory of Japan, 2-21-1 Osawa, Mitaka, Tokyo 181-8588, Japan*
[2]*Faculty of Science and Engineering, Kindai University, Higashi-Osaka, Osaka 577-8502, Japan*
[3]*Hiroshima University, 1-3-2 Kagamiyama, Higashi-Hiroshima City, Hiroshima 739-8511 , Japan*
[4]*Hiroshima Astrophysical Science Center, Hiroshima University, 1-3-1 Kagamiyama, Higashi-Hiroshima, Hiroshima 739-8526, Japan*
[5]*Core Research for Energetic Universe, Hiroshima University, 1-3-1, Kagamiyama, Higashi-Hiroshima, Hiroshima 739-8526, Japan*
[6]*INAF-Osservatorio Astronomico di Capodimonte, Via Moiariello 16, I-80131 Napoli, Italy*
[7]*Instituto de Astronomía y Ciencias Planetarias de Atacama, Universidad de Atacama, Av. Copayapu 485, Copiapó, Region de Atacama, Chile*

Accepted 2020 June 10. Received 2020 May 27; in original form 2020 January 5

ABSTRACT

We present a 23 deg^2 weak gravitational lensing survey of the Shapley supercluster core and its surroundings using *gri* VST images as part of the Shapley Supercluster Survey (ShaSS). This study reveals the overall matter distribution over a region containing 11 clusters at $z \sim 0.048$ that are all interconnected, as well as several ongoing cluster–cluster interactions. Galaxy shapes have been measured by using the Kaiser–Squires–Broadhurst method for the *g*- and *r*-band images and background galaxies were selected via the *gri* colour–colour diagram. This technique has allowed us to detect all of the clusters, either in the *g*- or *r*-band images, although at different σ levels, indicating that the underlying dark matter distribution is tightly correlated with the number density of the member galaxies. The deeper *r*-band images have traced the five interacting clusters in the supercluster core as a single coherent structure, confirmed the presence of a filament extending North from the core, and have revealed a background cluster at $z \sim 0.17$. We have measured the masses of the four richest clusters (A3556, A3558, A3560, and A3562) in the two-dimensional shear pattern, assuming a spherical Navarro–Frenk–White profile and obtaining a total mass of $\mathcal{M}_{\rm ShaSS,WL}=1.56^{+0.81}_{-0.55}\times10^{15}\,{\rm M}_\odot$, which is consistent with dynamical and X-ray studies. Our analysis provides further evidence of the ongoing dynamical evolution in the ShaSS region.

Key words: gravitational lensing: weak – galaxies: clusters: general – dark matter.

1 INTRODUCTION

Large-scale optical and spectroscopic explorations such as the Sloan Digital Sky Survey (York et al. 2000) have revealed the complex structures of the Universe – galaxy clusters, filaments, and voids. Superclusters represent the vastest coherent structures in the Universe, extending up to ∼100 across as observed in the wide optical surveys (e.g. Einasto et al. 2011). The observation of superclusters was often considered a challenge to the hierarchical structure formation paradigm since such extremely vast overdense structures, but also the largest voids, are not reproduced by the *N*-body simulations. However, new techniques to analyse *N*-body simulations (e.g. Yaryura, Baugh & Angulo 2011; Higuchi & Inoue 2019) obtained non-zero probabilities of identifying such peculiar systems (overdense and underdense) within redshift surveys. Recent numerical simulations (Einasto et al. 2019) showed that the stability of size and number of superclusters during their evolution are important properties of the cosmic web and that the number density of the superclusters thus constrains the cosmological models. Also, these structures are still collapsing with galaxy clusters and groups frequently interacting and merging, enhancing the effects of the environment on galaxy evolution. These effects are amplified in the supercluster high-density cores, which are gravitationally bound (Einasto et al. 2016) and anticipated to become the most massive virialized structures in the distant future. This implies that galaxy properties and the wider supercluster evolution are strongly related (e.g. Gray et al. 2009; Lubin et al. 2009; Mei et al. 2012; Merluzzi et al. 2016; Einasto et al. 2018; Galametz et al. 2018; Mahajan, Singh & Shobhana 2018).

The Shapley supercluster (SSC, $z \sim 0.05$) is the largest conglomeration of Abell clusters in the local Universe (see Fig. 1). At its heart there is a complex dense core consisting of five clusters forming a continuous filamentary structure 2° (∼8 Mpc; $H_0 = 70\,{\rm km\,s^{-1}\,Mpc^{-1}}$) in extent, that is filled with hot gas as seen by both Planck and *XMM–Newton* satellites (Planck Collaboration XXXI 2014; Merluzzi et al. 2016). Across this central region dynamical studies, X-ray, and radio observations showed evidence of multiple cluster–cluster interactions (e.g. Bardelli et al. 1998, 2000; Kull & Böhringer 1999; Venturi et al. 2003; Giacintucci et al. 2005; Miller 2005). Several attempts have also been undertaken to map the whole supercluster in order to determine its morphology

★ E-mail: yuichi.higuchi@nao.ac.jp

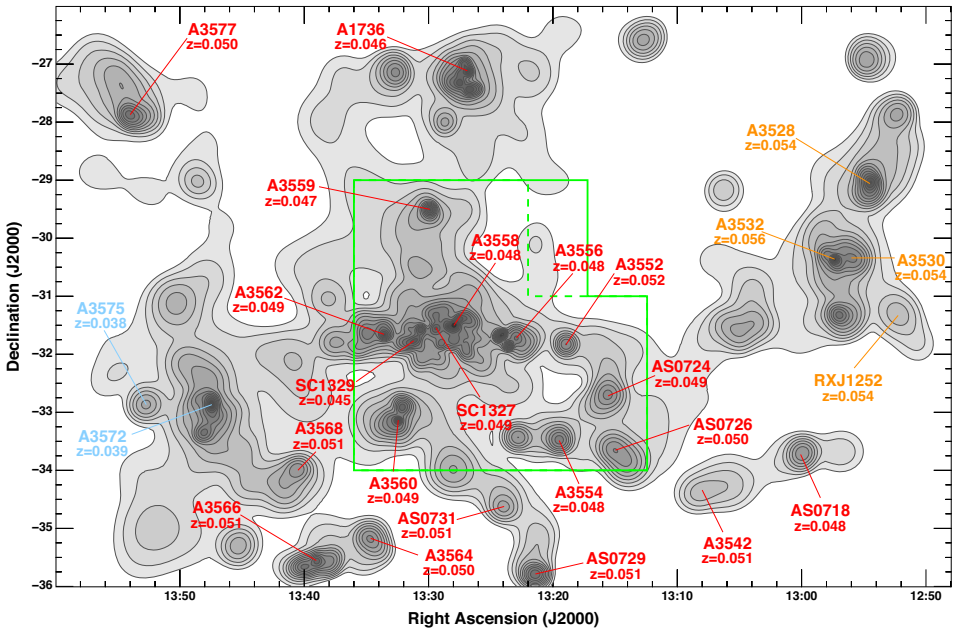

Figure 1. *K*-band luminosity-weighted density map of $0.035 \leq z < 0.060$ galaxies across the full extent of the SSC. *K*-band magnitudes are taken from the 2MASS Extended Source Catalogue and combine redshifts from the previous wide-field spectroscopic surveys covering the region (6dFGRS; Quintana et al. 1997; Kaldare et al. 2003; Drinkwater et al. 2004; Proust et al. 2006; Cava et al. 2009; Jones et al. 2009). Abell clusters within the same redshift range are labelled, colour coded in red is recession velocities within 1 500 km s^{-1} of the central cluster Abell 3558; in cyan is low-velocity extension $0.035 \leq z < 0.040$; and in orange is high-velocity wing, $0.053 \leq z < 0.060$. The solid green box outlines the 23 deg^2 region covered by ShaSS, and the dashed green lines our 21 deg^2 AAOmega survey (see the text).

and mass, as well as ascertain which portions of the supercluster were gravitationally bound (e.g. Reisenegger et al. 2000; Drinkwater et al. 2004; de Filippis et al. 2005; Proust et al. 2006; Muñoz & Loeb 2008). The supercluster resides in the direction of the cosmic microwave background (CMB) dipole anisotropy. Quintana et al. (1995) showed that the gravitational pull of the supercluster may account for 25 per cent of the peculiar velocity of the Local Group required to explain the anisotropy and their mass would be dominated by intercluster dark matter in that case, while the optical flux distribution lies ∼25° away from the CMB dipole. However, due to a lack of robust estimates of the SSC mass, the relevance of its gravitational pull upon the high peculiar velocity (∼600 km s^{-1}) of the Local Group relative to the Hubble Flow remains an open issue (Raychaudhury 1989; Kocevski, Ebeling & Mullis 2004; Courtois et al. 2017). An order of magnitude estimate of the SSC mass was provided by Reisenegger et al. (2000), by means of a dynamical analysis based on supercluster member galaxies. They estimated the mass of the central region within $8h^{-1}$Mpc of A 3558 to be $\mathcal{M} \sim 10^{16} h^{-1} \mathrm{M}_{\odot}$.

Although the previous studies were fundamental to demonstrate the complex dynamical status of the SSC, the lack of accurate and homogeneous multiband imaging and spectroscopic coverage across such an extended structure prevented, among other things, a quantitative description of the supercluster environment from filaments to cluster cores and a robust mass estimate.

With all this in mind, we have carried out the Shapley Supercluster Survey (ShaSS, Merluzzi et al. 2015), delivering high-quality optical and near-infrared imaging across a contiguous 23 deg^2 ($260\,h_{70}^{-2}$Mpc^2) region centred on the supercluster core. The survey includes nine Abell clusters (A 3552, A 3554, A 3556, A 3558, A 3559, A 3560, A 3562, AS 0724, AS 0726) and two poor clusters (SC 1327-312, SC 1329-313) whose redshifts all lie within 1500 km s^{-1} of Abell 3558 at $z = 0.048$ (see solid green box in Fig. 1 and refer for details to Merluzzi et al. 2015). The parameters of the clusters are given in Table 1 (see Haines et al. 2018).

The main objective of the ShaSS project is to investigate the role of cluster-scale mass assembly on the evolution of galaxies, mapping the effects of the environment in the cluster outskirts, and along the filaments with the aim of identifying the very first interactions between galaxies and their environment. In order to achieve this goal, it is crucial *to reveal the structure*, i.e. to obtain detailed maps of the dark matter and baryonic matter distributions (galaxies, intracluster medium), combining galaxy number and stellar mass density, weak lensing (WL), X-ray, and dynamical analyses. In this work, we characterized the supercluster environment by means of WL technique.

While we have been able to produce highly detailed and complete two-dimensional density maps of the galaxy distribution across the SSC (Haines et al. 2018) and the stellar mass content (Merluzzi et al. 2015), this stellar content is expected to only represent a relatively small fraction of the global mass of this region, in comparison to the hot X-ray emitting gas of the clusters and the wider dark matter component. More problematically, the relative fraction of baryonic component that is locked into stars and galaxies rather than hot gas, and the global mass-to-light ratios have been shown to vary significantly between galaxy groups and the most massive clusters, with galaxy groups much more efficient at converting the baryons into stars and producing light than clusters (e.g. Tully 2005; Gonzalez, Zaritsky & Zabludoff 2007; Gonzalez et al. 2013). Thus, it is no trivial matter to translate the galaxy distribution or stellar mass distribution to the wider mass distribution.

Table 1. Properties of the 11 known X-ray galaxy clusters in the SSC. The central velocities $\langle V_h \rangle$, velocity dispersions σ_v, number of spectroscopic members within r_{200} (N_z), and r_{200} radii (in Mpc) are all determined by Haines et al. (2018). *ROSAT*-based X-ray bolometric luminosities taken from de Filippis, Schindler & Erben (2005), except A 3559, A 3560 from Ettori, Fabian & White (1997). The last column lists the dynamical masses derived from the analysis of Haines et al. (2018).

Cluster Name	RA (J2000) (°)	Dec. (J2000) (°)	$\langle V_h \rangle$ (km s^{-1})	σ_v (km s^{-1})	N_z	r_{200} (Mpc)	$L_{X,\,bol}$ 10^{43} (erg s^{-1})	$\mathcal{M}_{dyn}$ (10^{13} M$_\odot$)
AS 0724	198.863 788	−32.710 022	14 748 ± 74	410 ± 41	29	0.945	1.5	10.06 ± 3.02
AS 0726	198.655 892	−33.764 558	14 911 ± 94	603 ± 48	38	1.397	0.7	32.40 ± 7.74
Abell 3552	199.729 560	−31.817 560	15 777 ± 75	334 ± 42	19	0.769	0.4	5.41 ± 2.04
Abell 3554	199.881 979	−33.488 139	14 346 ± 66	602 ± 37	77	1.387	2.0	31.67 ± 5.84
Abell 3556	201.028 020	−31.669 858	14 396 ± 45	628 ± 31	257	1.447	1.7	35.94 ± 5.32
Abell 3558	201.986 896	−31.495 847	14 500 ± 39	1007 ± 25	867	2.319	66.8	148.16 ± 13.72
Abell 3559	202.462 154	−29.514 386	14 149 ± 63	521 ± 39	68	1.201	1.5	20.59 ± 4.62
Abell 3560	203.107 354	−33.135 989	14 739 ± 52	860 ± 32	304	1.981	11.7	92.29 ± 10.30
Abell 3562	203.402 575	−31.670 383	14 786 ± 53	769 ± 30	198	1.770	33.1	65.87 ± 7.71
SC 1327-312	202.448 625	−31.602 450	14 794 ± 38	535 ± 17	220	1.347	12.7	29.84 ± 2.84
SC 1329-313	202.913 761	−31.807 260	13 416 ± 49	373 ± 28	55	0.862	5.2	7.60 ± 1.71

Weak gravitational lensing enables the overall mass distribution of clusters and superclusters to be directly measured without requiring us to make any assumptions regarding the dynamical state of the system (Einasto et al. 2003; Oguri et al. 2004). The tidal gravitational field of a cluster leads to the differential deflection of light coming from background galaxies, distorting them, and producing a coherent shear signal on top of the random intrinsic ellipticities of individual galaxies. Measuring this coherent distortion pattern among the background galaxies enables the two-dimensional mass distribution of the cluster/supercluster to be mapped (e.g. Medezinski et al. 2010; Oguri et al. 2012; Umetsu et al. 2014). This technique is particularly powerful for those unvirialized regions beyond the cluster core, where traditional approaches based on galaxy dynamics or X-ray emission are no longer suitable. WL analyses have been used to detect filamentary structures connecting adjacent galaxy clusters (Heymans et al. 2008; Dietrich et al. 2012; Higuchi, Oguri & Shirasaki 2014), or provide mass maps of merging cluster systems (e.g. Okabe & Umetsu 2008; Jee et al. 2014).

In a previous study applying a lensing analysis to superclusters, we showed the correlation between the early-type galaxy distribution and WL density map in the central $\sim$1 deg^2 region, including A 3558 and SC 1327-312. We measured for the mass of A 3558 $\mathcal{M}_{500} = 7.63^{+3.88}_{-3.40} \times 10^{14}\,\mathrm{M}_\odot$ consistent with that derived from the X-ray observations $\mathcal{M}_{500} = (4.62 \pm 0.24) \times 10^{14}\,\mathrm{M}_\odot$ (Merluzzi et al. 2015). The agreement of the two independent measurements demonstrated the feasibility and effectiveness of the WL analysis, which we will here extend and improve considering the whole ShaSS region.

Beyond deriving cluster masses using a complementary approach, the WL technique will enable us to further investigate the nature of the whole system, tracing the mass distribution outside of the cluster cores, as well as revealing possible background structures. In particular, in Haines et al. (2018) with the galaxy number density map and the dynamical analysis, we established the existence of a stream of galaxies connecting A 3559 to the supercluster core. Moreover, the updated central redshifts and velocity dispersions of the 11 clusters confirmed that they all lie within 1300 km s^{-1} of the central cluster A 3558. These 11 systems are all interconnected and lie within a coherent sheet of galaxies that fills the entire survey region without gaps. Clear velocity caustics extend right to the survey boundary, indicating that the entire structure is gravitationally bound and in the process of collapse. All this invokes and supports a deeper examination.

The structure of the paper is organized as follows. Section 2 describes the main characteristics of the data set. Section 3 introduces the basics of WL and the methods of analysis. The shear measurement, background galaxies selection, and fitting procedure are detailed in Section 4. Section 5 presents the results of the WL analysis, which are discussed in Section 6. Lastly, Section 7 summarizes our findings.

We adopt the following cosmological parameters: the *Hubble* parameter $H_0 = 70\,\mathrm{km\,s^{-1}\,Mpc^{-1}}$, the density parameter of total matter $\Omega_m = 0.3$, $\Omega_\Lambda = 0.7$, spectral index $n_s = 0.972$ and density fluctuation amplitude $\sigma_8 = 0.823$, assuming a flat FLRW cosmology. Otherwise, $h = H_0/100$.

2 THE DATA

The ShaSS data base consists of high-quality optical *ugri* imaging acquired with OmegaCAM (Kuijken 2011) on the 2.6-m VLT Survey Telescope (VST, Capaccioli & Schipani 2011) and near-infrared *K*-band imaging from the 4.1-m Visible and Infrared Survey Telescope for Astronomy, both taking advantage of the exceptional observing conditions available at Cerro Paranal in Chile. In addition, our ad hoc spectroscopic survey carried out with the AAOmega spectrograph on the 3.9-m Anglo Australian Telescope provides highly complete and homogeneous redshift coverage across the full ShaSS region (see Haines et al. 2018).

The corrected OmegaCAM field of view of 1 × 1 deg^2 allows the whole ShaSS area to be covered with 23 VST fields, sampled at 0.21 arcsec-per-pixel corresponding to a sub-kiloparsec resolution at the supercluster redshift. Each of the contiguous ShaSS fields is observed in four bands: u (t_{exp} = 2955 s), g (1400 s), r (2664 s), and i (1000 s), reaching 5σ (AB) magnitude limits of 24.4, 24.6, 24.1, and 23.3, respectively (see Mercurio et al. 2015; Merluzzi et al. 2015). The r-band images were to be acquired in the best-seeing conditions with the aim of using these data for shear measurements and morphological classification. The median seeing in r band is 0.6 arcsec, corresponding to 0.56 kpc at $z = 0.048$.

The VST images have been processed and photometrically calibrated using the VST-Tube pipeline (Grado et al. 2012), and the catalogue produced as described in Mercurio et al. (2015). In

Table 2. List of the parameters from the *gri* catalogues that were used to perform the WL analysis.

Parameter	Units	Description
ID		ShaSS identification
RA	deg	Right Ascension (J2000)
DEC	deg	Declination (J2000)
MK	mag	Kron magnitude
EMK	mag	Error on Kron magnitude
MA_{15}	mag	Aperture magnitude inside 1.5- arcsec diameter
EMA_{15}	mag	Error on aperture magnitude inside 1.5 -arcsec diameter
MPSF	mag	Magnitude resulting from the PSF fitting
EPSF	mag	Error on magnitude resulting from the PSF fitting
SG		Star/galaxy separation
HFF		Halo fraction flag
HF		Halo flag value
SFF		Spike fraction flag
SF		Spike flag value

each band, the complete catalogues contain a wealth of information. Table 2 lists the parameters from the catalogues that have been used for the WL analysis. Both the Kron magnitudes (*MK*, Kron 1980) and the 1.5 -arcsec aperture magnitudes (MA_{15}) were corrected for Galactic extinction following Schlafly & Finkbeiner (2011).

Since multiple reflections in the internal optics of OmegaCAM can produce complex image rings and ghosts (hereafter star haloes) near bright stars, we carefully traced the effects of such features on source detection (for details see Mercurio et al. 2015). In addition, the saturated stars with haloes also affect the images by producing spike features which are identified. The parameters *HFF*, *HF*, *SFF*, and *SF* in Table 2 are indicative of the robustness of the photometry. *HF* (*SF*) greater than 0 marks that the source is at least partially affected by the halo (spike) of a bright star and indicates the star magnitudes (spike strength). While *HFF* (*SFF*) *measures* the fraction of the source area affected by the halo (spike). Finally, the *SG* parameter identifies galaxies ($SG = 0$) and stars ($SG > 0$). The saturated stars ($SG = 9$) are also indicated. In the following analysis, we excluded all the sources with HF or SF greater than 0, i.e. all the sources even marginally affected by haloes or spikes, as well as saturated stars.

The survey was designed to study the galaxy population down to $m^\star + 6$ at supercluster redshift ($m_r^\star = 15$ mag in AB magnitudes). With this precondition, we fixed the required depth in each band using typical galaxy colours at $z \sim 0.05$ according to stellar population models (e.g. Bruzual & Charlot 2003). Further constraints were placed by (i) the morphological classification based on the *r*-band imaging, which requires a signal-to-noise ratio about 100[1] and (ii) the plan to use *r*-band imaging for the WL analysis. This translates in photometric catalogues having different magnitude limits in the different bands, with the *r*-band catalogue including the fainter sources in the ShaSS field.

It follows that to maximize the number density of sources for the background galaxy selection (see Section 4) and the photometric redshift estimate, we take advantage of the deeper *gri* catalogues. The three catalogues have been cross-correlated using *STILTS*[2] with the *r*-band catalogue as reference table and keeping only the sources detected in all the three bands.

[1]For the global galaxy properties a signal-to-noise ratio about 10–20 is instead sufficient.
[2]http://www.star.bris.ac.uk/mbt/stilts/

The *g*-band imaging is generally used for the WL mass measurement presented here, together with the *gri* catalogues and the spectroscopic catalogue. Although the *r*-band imaging is deeper, the *r*-band imaging was found to present significant distortions in some restricted regions, and thus the *g*-band imaging was used as an alternative source of shear measurements. For this reason, and to provide consistency checks across the wider WL maps, the WL analysis was carried out in both *r* and *g* bands.

The spectroscopic survey was carried out using the AAOmega multifiber spectrograph on the 3.9-m Anglo-Australian telescope, collecting redshift measurements for 4027 galaxies (Haines et al. 2018). Targets were selected from the VST images as having $i < 18.0$ (AB) and WISE/W1 < 15.5 mag (Vega). There have also been multiple previous redshift surveys of the region, and combining these literature redshifts with our own, results in redshifts being known for 95 per cent of all $i < 18$, W1 < 15.5 galaxies (5689/6008) across the whole survey region. The redshift distribution of the non-SSC galaxies has the typical form of magnitude-limited samples (e.g. Jones et al. 2009), with a median redshift of 0.138 and 95 per cent of galaxies within the range 0.014–0.295. This permits background structures connected to the WL peaks to be reliably identified and mapped in redshift-space out to $z \sim 0.3$.

3 ANALYSIS METHODS

3.1 Navarro–Frenk–White (NFW) model

Simulations and observational results revealed that the halo density profile is inversely proportional to the distance *r* from the cluster centre inside a scale radius r_s, and proportional to r^{-3} outside this radius. This profile is called NFW profile (Navarro, Frenk & White 1997), defined by

$$\rho(r) = \frac{\delta_c \rho_c}{r/r_s(1 + r/r_s)^2}, \quad (1)$$

where ρ_c is the critical density of the Universe at the cluster redshift. The characteristic overdensity is described with the concentration parameter $c = r_{200}/r_s$ by

$$\delta_c = \frac{200}{3} \frac{c^3}{\ln(1 + c) - c/(1 + c)}, \quad (2)$$

where r_{200} is defined as the radius inside which the mass density of the halo is equal to 200 times the critical density. The scale radius

can be derived from the mass of the halo M_{200} and the concentration parameter as

$$r_{\rm s} = \left(\frac{3M_{200}}{800\pi\rho_{\rm c}}\right)^{1/3} c. \tag{3}$$

Therefore, the density profile can be determined as a function of mass and concentration parameter when the halo redshift is known.

3.2 Concentration and mass relation

N-body simulations and observational results show that halo mass is correlated with the concentration parameter (Jing 2000; Bullock et al. 2001; Zhao et al. 2009; Oguri et al. 2012; Umetsu et al. 2014). The concentration and mass relation (hereafter, *c*–*M* relation) can be modelled with four parameters: $M_{\rm piv}$, A, B, and C at a redshift of z (Duffy et al. 2008) as

$$c = A\left(\frac{M_{200}}{M_{\rm piv}}\right)^{B}(1+z)^{C}. \tag{4}$$

In the following analysis, we used $M_{\rm piv} = 2\times10^{12}h^{-1}{\rm M}_{\odot}$, $A = 7.85$, $B = -0.081$, and $C = -0.71$ that were obtained by fitting haloes in the *N*-body simulation (Duffy et al. 2008).

3.3 Lensing equations

The three-dimensional potential $\Phi(D_{\rm d}\theta, z)$ of a lens is related to the lensing potential $\psi(\theta)$ on the sky plane as

$$\psi(\theta) = \frac{2D_{\rm ds}}{c^2 D_{\rm d} D_{\rm s}}\int {\rm d}z\Phi(D_{\rm d}\theta, z), \tag{5}$$

where θ is a position vector on the sky plane and c is the speed of light. $D_{\rm d}$, $D_{\rm s}$, and $D_{\rm ds}$ are the angular diameter distances between the observer and the lens, the observer and the sources, and between the lens and the sources, respectively . Given the cluster properties, the convergence and shear for the NFW profile can be obtained as the derivatives of the lens potential. The potential is related to the shear as

$$\gamma_1(\theta) = \frac{1}{2}\left(\frac{\partial^2\psi(\theta)}{\partial\theta_1^2} - \frac{\partial^2\psi(\theta)}{\partial\theta_2^2}\right), \tag{6}$$

$$\gamma_2(\theta) = \frac{\partial^2\psi(\theta)}{\partial\theta_1\partial\theta_2}. \tag{7}$$

For spherically symmetric objects, the direction of shear has only a tangential component. It is useful to define the tangential γ_+ and cross $\gamma_{\rm x}$ components for γ_1 and γ_2 as

$$\begin{pmatrix}\gamma_+\\ \gamma_{\rm x}\end{pmatrix} = \begin{pmatrix}-\cos2\phi & -\sin2\phi\\ -\sin2\phi & \cos2\phi\end{pmatrix}\begin{pmatrix}\gamma_1\\ \gamma_2\end{pmatrix}, \tag{8}$$

where ϕ is the angle between the galaxy position and θ_1 axis. The shear profile for the spherical symmetric NFW profile can be written as a function of the distance from the centre by (Wright & Brainerd 2000; Bartelmann & Schneider 2001)

$$\gamma_+(x) = \frac{r_{\rm s}\delta_{\rm c}\rho_{\rm c}}{\Sigma_{\rm c}}\left[\frac{10}{3} + 4\ln\left(\frac{1}{2}\right)\right] \qquad (x=1),$$

$$\frac{r_{\rm s}\delta_{\rm c}\rho_{\rm c}}{\Sigma_{\rm c}}\left[\frac{8{\rm arctanh}\sqrt{(x-1)/(1+x)}}{x^2\sqrt{x^2-1}} + \frac{4}{x^2}\ln\left(\frac{\rm x}{2}\right)\right.$$

$$\left. - \frac{2}{x^2-1} + \frac{4{\rm arctanh}\sqrt{(x-1)/(1+x)}}{(x^2-1)^{3/2}}\right] \quad (x<1), \tag{9}$$

where x is a scaled radius defined by $x = R/r_{\rm s}$. R is a distance on the sky plane, defined as $R = D_{\rm d}\sqrt{\theta_1^2+\theta_2^2}$. From observations, we can only obtain the reduced shear defined by

$$g_\alpha = \frac{\gamma_\alpha}{1-\kappa}, \tag{10}$$

where α takes the values of 1 or 2 for each shear component and κ is the convergence.

In this study, we measured cluster properties in the two-dimensional plane following Oguri et al. (2010) and Okabe et al. (2010). We divided the sky into pixels. Then we calculated the average shear value at each pixel, which is obtained at a position θ by

$$\langle g_\alpha\rangle(\theta) = \frac{\sum_{i=1}^{N} w_i g_{\alpha,i}(\theta_i)}{\sum_{i=1}^{N} w_i}, \tag{11}$$

where θ_i is the position of the ith source galaxy in the pixel. The weight for the ith galaxy is defined by

$$w_i = \frac{1}{\sigma_{{\rm e},i}^2 + \Delta^2}. \tag{12}$$

$\sigma_{{\rm e},i}$ is a shape measurement error for the ith galaxy. We used $\Delta = 0.4$ through this paper. The shape measurement error for a pixel is obtained as

$$\sigma_{\rm e}^2 = \frac{\sum_{i=1}^{N}\left(w_i\sigma_{{\rm e},i}\right)^2}{\left(\sum_{i=1}^{N} w_i\right)^2}. \tag{13}$$

3.4 Covariance matrix

In order to fit the cluster profiles with the NFW profile, we calculated the chi-square value for each parameter estimation step, defined as

$$\chi^2 = \sum_{\alpha,\beta=1}^{2}\sum_{k,l=1}^{N_{\rm pixel}}\left[g_\alpha(\theta_k) - g_\alpha^{\rm model}(\theta_k)\right]C^{-1}_{\alpha\beta,kl} \times\left[g_\beta(\theta_l) - g_\beta^{\rm model}(\theta_l)\right], \tag{14}$$

where $g^{\rm model}(\theta_k)$ is the model value for a given parameter set at a position θ_k and $N_{\rm pixel}$ is the number of pixels. C^{-1} is the inverse covariance matrix. In the estimation of the covariance matrix, we took into account the contribution from the shape noise $C^{\rm shape}$ and large-scale structures $C^{\rm LSS}$:

$$C = C^{\rm shape} + C^{\rm LSS}. \tag{15}$$

Assuming that the ellipticities of galaxies are not correlated, the covariance matrix term for the shape noise is estimated with equation (13) as

$$C^{\rm shape}_{\alpha\beta,kl} = \sigma_{\rm e}^2(\theta_k)\,\delta^K_{\alpha\beta}\delta^K_{kl}, \tag{16}$$

where δ^K is the Kronecker delta function. The covariance matrix for large-scale structures can be estimated as

$$C^{\rm LSS}_{\alpha\beta,kl} = \xi_{\alpha\beta}(\theta), \tag{17}$$

where $\xi(\theta)$ is the cosmic shear correlation function. We assumed the correlation function depends only on the distance between the galaxy positions. Each component of the shear correlation function is calculated as (Bartelmann & Schneider 2001; Umetsu et al. 2011, 2016)

$$\xi_{11}(\theta) = \frac{1}{2}\int \frac{ldl}{2\pi} P_\kappa(l)\,[J_0(l\theta) + J_4(l\theta)\cos(4\phi)]\,,$$

$$\xi_{22}(\theta) = \frac{1}{2}\int \frac{ldl}{2\pi} P_\kappa(l)\,[J_0(l\theta) - J_4(l\theta)\cos(4\phi)]\,,$$

$$\xi_{12}(\theta) = \frac{1}{2}\int \frac{ldl}{2\pi} P_\kappa(l)\,J_4(l\theta)\sin(4\phi)\,, \tag{18}$$

where $J_{0,4}$ are the zeroth- and fourth-order Bessel functions, respectively, and $P_\kappa(l)$ is the convergence power spectrum.

4 SHAPE MEASUREMENT AND SOURCE GALAXY SELECTION

The shapes of galaxies were measured using the KSB method (Kaiser, Squires & Broadhurst 1995), with some modifications (see Umetsu et al. 2010; Oguri et al. 2012; Okabe et al. 2013, 2014, 2016) in both *g*- and *r*-band imaging. Image ellipticity was derived from the weighted quadruple moments of the surface brightness of objects. The data region of each pointing was divided into several rectangular blocks based on the typical coherent scale of the measured PSF anisotropy pattern (e.g. Okabe et al. 2016). We selected bright unsaturated stars in the half-light radius, r_h–magnitude plane to estimate the stellar anisotropy kernel, $q^*_\alpha = (P^*_{\rm sm})^{-1}_{\alpha\beta} e^\beta_*$. $P^{\alpha\beta}_{\rm sm}$ is the smear polarisability matrix. e_α is the image ellipticity. Quantities with an asterisk denote those for stellar objects. We corrected the PSF anisotropy with the equation

$$e'_\alpha = e_\alpha - P^{\alpha\beta}_{\rm sm} q^*_\beta. \tag{19}$$

We estimated $q^*_\alpha(\theta)$ at each galaxy position, θ, by using as a fitting function second-order bi-polynomials of the vector θ with iterative σ-clipping rejection. Since the PSF distortion pattern in the VST data is locally variable, we carried out star and galaxy separation in each rectangular block. We then calibrated the KSB isotropic correction factor for individual objects using a subset of galaxies detected with high significance $\nu > 50$. The isotropic PSF calibration was also carried out in the individual blocks used for the anisotropic PSF correction. We checked the ellipticities for galaxies detected over different pointings and found a general agreements. We then adopted the average of the ellipticity for the WL mass measurement with the weight of equation (12).

The redshift of each galaxy in the *gri* ShaSS photometric catalogues was estimated by using the COSMOS photometric redshift catalogue (Ilbert et al. 2013). We first computed the lensing kernel, $\beta_i \equiv D_{{\rm ds},i}/D_{{\rm s},i}$, of the i th galaxy as an ensemble average of the N nearest neighbours in the *gri*−magnitude space of the jth galaxy in the COSMOS catalogue:

$$\beta_i = \langle D_{\rm ds}/D_{\rm s}\rangle_{\rm COSMOS} = \frac{1}{N}\sum_j^N D_{{\rm ds},j}(z_{\rm s})/D_{{\rm s},j}(z_{\rm s}). \tag{20}$$

We then assigned the redshift of each galaxy from β_i, where we adopted $N = 50$.

To define the foreground and background galaxies, we used the distance ratio in the colour–colour diagram. Fig. 2 shows the mean distance ratio in the colour–colour diagram. In the map, we divided the diagram into cells and calculated the mean value in each pixel.

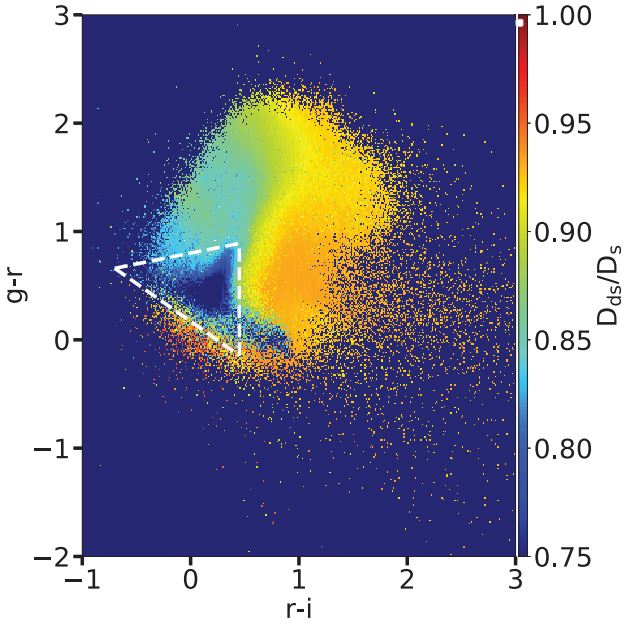

Figure 2. Ratio $D_{\rm ds}/D_{\rm s}$ of the distances between the observer and the sources and the lens and the sources in the colour–colour diagram. The horizontal axis shows $r - i$. The vertical axis shows $g - r$. Colour indicates the mean value of $D_{\rm ds}/D_{\rm s}$ in each pixel. The galaxies inside the triangle region are defined as the foreground and cluster member galaxies.

As seen in Fig. 2, there is a clump having the low value, which corresponds to the cluster members and foreground galaxies. In order to exclude such galaxies, we defined the region residing in the clump as

$$g - r < 0.2(r - i) + 0.8\,(\text{for } -0.4 \le r - i \le 0.3), \tag{21}$$

$$g - r > -0.7(r - i) + 0.17\,(\text{for } -0.4 \le r - i \le 0.3), \tag{22}$$

$$r - i < 0.45\,(\text{for } 0.17 \le g - r \le 0.63). \tag{23}$$

To exclude the effects from bright stars on the shape measurement of the galaxies, we did not use galaxies which were closer than one star half-light radius from the brightest (<18 mag) stars. Moreover, we only used the galaxies between $r = 21.5$ and 24.5 mag. We could not find large dependence of shear profiles on the selection criteria and the magnitude of the bright stars. After adopting these cuts, the number density of galaxies for the shear measurement becomes $n_g = 7$ arcmin^{-2}. Fig. 3 shows the redshift distribution for galaxies between $i = 21.5$−24.5 mag before (dotted line) and after adopting the selection criteria (solid line). We can see that galaxies at lower redshifts are eliminated by adopting the colour cut. As a result, the mean source redshift weighted by the estimated errors of $D_{\rm ds}/D_{\rm s}$ becomes $z_{\rm s} = 0.81$ after the colour cut.

5 RESULTS

5.1 WL mass reconstruction

We reconstructed the projected mass distribution, the so-called mass map, by following Kaiser & Squires (1993), Okabe & Umetsu (2008). We employed a Gaussian smoothing scale of FWHM = 10 arcmin. Fig. 4 shows the WL mass map (contours) of the Shapely supercluster region for *r* and *g* bands, respectively. The errors were estimated by a bootstrap realization ($N = 10\,000$), which randomly rotates galaxy

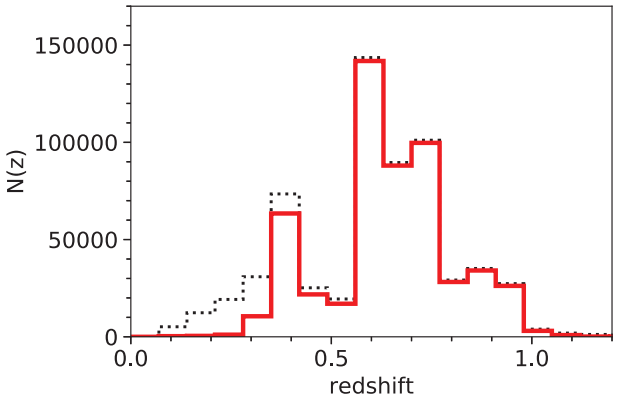

Figure 3. Redshift distribution of the source galaxies. The horizontal axis shows the redshift. The vertical axis shows the number count. We only used galaxies whose *i*-band magnitudes are between 21.5 and 24.5. The dotted line shows its distribution before adopting the selection criteria for the background galaxy. The solid line shows the result after adopting the criteria. The weighted mean redshift is 0.81.

orientations with fixed positions. The colours in the figures showed the galaxy number density derived from Haines et al. (2018). The WL mass distribution is highly associated with the spatial distribution of SSC member galaxies (see Fig. 4). In particular, we find significant peaks around A 3556, A 3558, SC 1327-312, SC 1329-313, A 3562, and A 3559 in both *r*- and *g*-band images. Less pronounced peaks are associated with A 3560 and A 3554 in the *g*-band images, where a marginal detection of A 3552 is also present. The lack of WL signal in *r*-band images for the cluster A 3560 can be explained with the peculiar distortion affecting the *r*-band images of this VST field. On the other hand, AS 0724 seems to be detected only in the *r*-band images. We could not find instead a clear peak around AS 0726 neither in the *r*- nor the *g*-band images.

Some of the mass peaks without any adjacent overdensity in supercluster galaxies are associated with background components (see Section 6). Therefore, our mass map is reasonably explained by the superposition of the supercluster component and background structures.

5.2 Fitting with the NFW profile

To estimate the mass and concentration parameters for each cluster, we fitted the shear values with the NFW profile on a two-dimensional shear map. Due to the shape measurement problem, we could not derive the properties of the individual low-mass clusters from the fitting. Therefore, the two-dimensional fitting was carried out only for the most massive clusters A 3556, A 3558, A 3560, and A 3562 (see Table 1). We simultaneously fitted the three clusters A 3556, A 3558, and A 3562 by assuming three NFW profiles. The cluster A 3560, which was far from the three clusters, was also fitted in the two-dimensional plane independently. On the other hand, we measured the tangential shear profiles for each low-mass cluster, and derived their mass and concentration parameters. Moreover, we stacked the shear profiles to investigate the average properties of the low-mass clusters.

In the two-dimensional fitting, we selected galaxies in the range of $200.3 \leq \mathrm{RA} \leq 203.8$ and $-32.1 \leq \mathrm{Dec.} \leq -31.1$ for the analysis of A 3556, A 3558, and A 3562. For A 3560, galaxies in the range of $202.6 \leq \mathrm{RA} \leq 203.6$ and $-33.6 \leq \mathrm{Dec.} \leq -32.6$ were instead used. The selected regions were divided into cells with the pixel scale of 3 arcmin on a side. We calculated a shear value in each pixel by following equation (11). In the fitting, we used the positions of the brightest cluster galaxies (BCG) as the centres of the clusters. We ran the Markov chain Monte Carlo (MCMC) by parametrizing masses and concentration parameters. For analysis of the three clusters (A 3556, A 3558, and A 3562), we searched the best-fitted parameters for each clusters simultaneously. In order to get the best fitted parameters from the chain distribution, we used the software `ChainConsumer` (Hinton 2016). We also carried out the fitting for the cluster A 3560 independently.

In the calculation of the covariance matrix, we assumed that source galaxies are present at the average source redshift of the background galaxies. Since the ShaSS area is large, we only used the diagonal terms of the covariance matrix to reduce the computational time in the fitting. We searched the best-fitting parameters in the range $10^{13}\mathrm{M}_{\odot} \leq M_{200} \leq 10^{16}\mathrm{M}_{\odot}$ and $0.5 \leq c \leq 15$. In order to check the effect of the pixel scale, we also ran the MCMC for the pixel scale of 2 and 4 arcmin, respectively. The obtained results were consistent with those for 3 arcmin within 2σ. Moreover, we derived the masses for the r −band data. However, the obtained results are consistent with the masses estimated by *g*-band data within 2σ. In addition, we also added the centres of the clusters as parameters for the fitting. We searched the centres within 5 armin from the positions from the BCGs. However, the offset between obtained centres and the positions of the BCGs were within a few arcmin while the centre for A 3560 did not converge. The differences for the other parameters were consistent within the error bar even in this case. Figs 5 and 6 show the MCMC results for A 3556, A 3558, and A 3562, and A 3560, respectively. Table 3 summarizes the results. For A 3562, the estimation for the concentration parameter did not converge, presumably because the off-centring between the position of the BCG and the WL centre or large noises in galaxy shapes.

For the clusters with lower masses (AS 0724, A 3552, A 3554, A 3559, SC 1327-312, and SC 1329-313), we fitted their tangential shear profiles with the NFW profile in 11 annular bins from the BCG position out to 30 arcmin. In order to check the effects of the bin size on the obtained parameters, we increased and decreased the number of bins and fitted their profiles. We find that the results turn out to be consistent within the errors. The derived best-fitting parameters are summarized in Table 4. Due to the low lensing signal, the fit does not converge for AS 0726. Fig. 7 shows the measured tangential and cross-shear profiles with the best-fitted NFW profile for each cluster.

For comparison and to investigate the average properties of the low-mass clusters, we also fitted the tangential shear profile obtained by stacking the shear profiles of the individual clusters weighted with the errors. In the stacking analysis, we included the profile of the cluster A 0726 and stacked the seven low-mass clusters.

Fig. 8 shows the stacked shear profile with the best-fitted profile. The estimated parameters are $M_{200} = (2.45^{+3.12}) \times 10^{13} h^{-1}\mathrm{M}_{\odot}$ and $c = 3.68^{+6.44}$. The large error is mainly caused by the small number of background galaxies.

6 DISCUSSION

6.1 WL mass map revealing the supercluster and background structures

In Fig. 4, we showed the number density map of supercluster galaxies across the ShaSS as derived by Haines et al. (2018), superimposed with the contours of the WL mass maps obtained from the *r*- (upper panel) and *g*-band (lower panel) imaging. As already noted, both the WL maps show an overall agreement with the structure as traced by the galaxy number density, albeit with a few divergences due to either

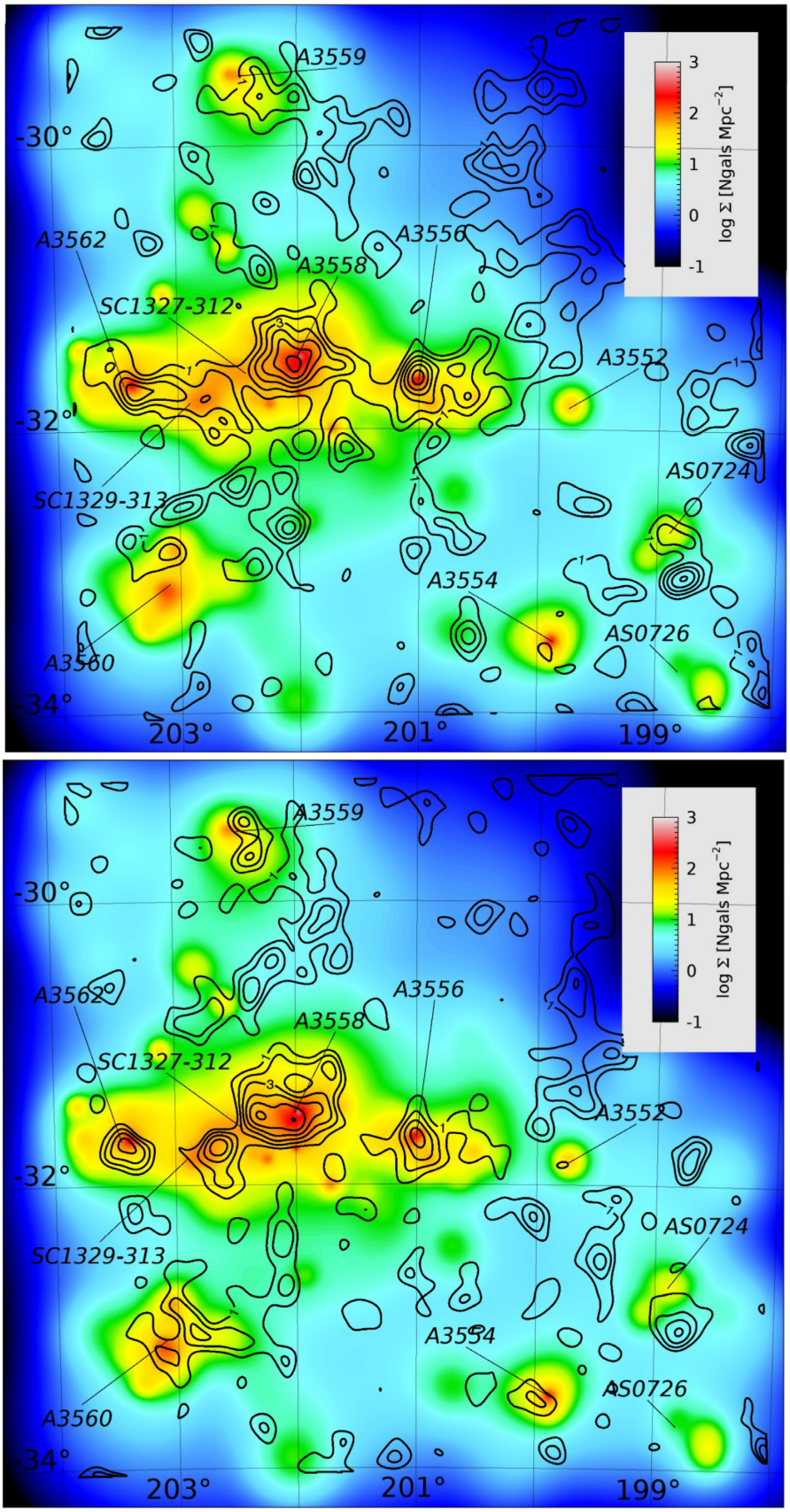

Figure 4. Galaxy number density from Haines et al. (2018) colour-coded as indicated in the right bar and with overlaid the contours of WL mass map as derived using the *r*-band imaging (upper panel) and *g*-band imaging (lower panel). The overlaid contours are stepped by 1σ from 1σ.

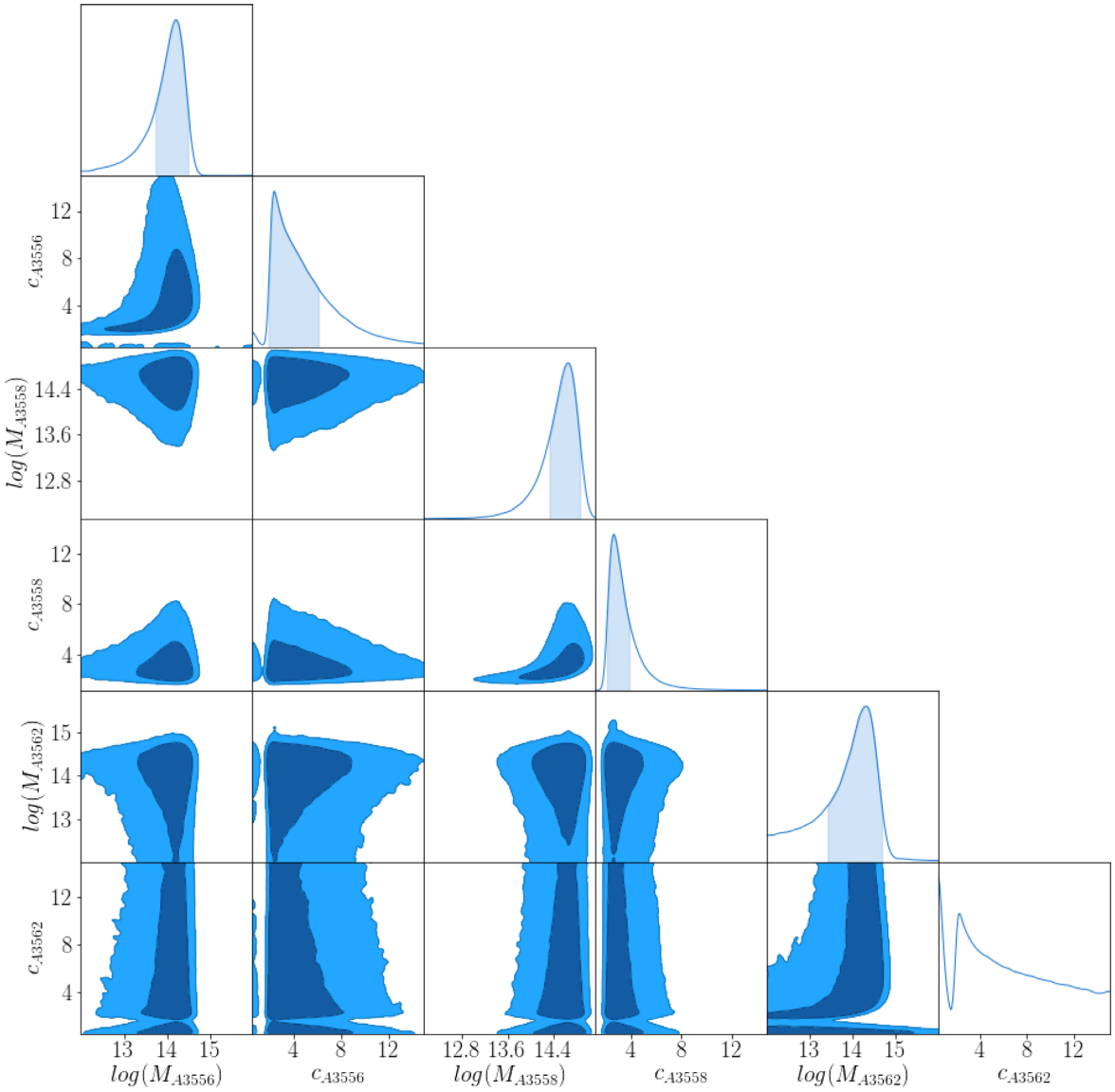

Figure 5. MCMC results for A 3556, A 3558, and A 3562 with a pixel scale of 3 arcmin. The horizontal axis shows mass M_{200} in units of $(h^{-1}\mathrm{M}_{\odot})$. The vertical axis shows concentration parameter. Contours are stepped by 1σ.

the different depths or distortions affecting certain fields. Both the WL maps well trace the supercluster core including the five clusters. In particular, the WL map obtained with *r*-band imaging shows a continuous structure between the five clusters at the 1σ level (upper panel in Fig. 4).

Merluzzi et al. (2015) and Haines et al. (2018) found a filament in the galaxy distribution which connects A 3559 to the centre of the supercluster. The density contrast of filaments being so low (Maturi & Merten 2013; Higuchi et al. 2014), it is difficult to significantly detect such a structure in our analysis; however, the WL contours have a trend to follow the filament connecting A 3559 to the supercluster core.

The WL mass maps also reveal a number of peaks that do not appear to be associated with any known cluster within the SSC. These peaks could instead be due to clusters located behind the SSC.

We take advantage of our extensive spectroscopic coverage of the entire ShaSS region to investigate the nature of these peaks. The *r*-band WL mass reconstruction shows an $\sim 4\sigma$ mass peak at RA = 202.°1, Dec. = –32.°7 that is not located near to any of the SSC clusters or any plausible grouping of SSC member galaxies. An examination of the redshifts of galaxies in the immediate vicinity of the WL peak reveals that the nine nearest galaxies ($d < 160$ arcsec) all have $z \sim 0.177$, with a further nine $z \sim 0.177$ galaxies located within 8 arcmin. The *gri* colour composite image of the region (Fig. 9) shows that the WL peak (blue contours) is centred on this dense concentration of red-sequence galaxies, which are confirmed to lie within the redshift range $0.173 < z < 0.182$ (white squares). The lower panel shows the corresponding distribution of galaxies in the caustic diagram, plotting recession velocity (V_{h}) versus projected distance from cluster centre (defined by the peak in the WL map), confirming that cluster membership is well defined for this $z \sim 0.177$ system, with noticeable velocity gaps above 54 500 km s^{-1} and below 51 700 km s^{-1} where no galaxies are seen within 1.5 Mpc of the cluster centre. The biweight estimator (Beers, Flynn & Gebhardt 1990) was used to derive a central recession velocity of 51 155 km s^{-1} ($z = 0.1773$) for the cluster and a velocity

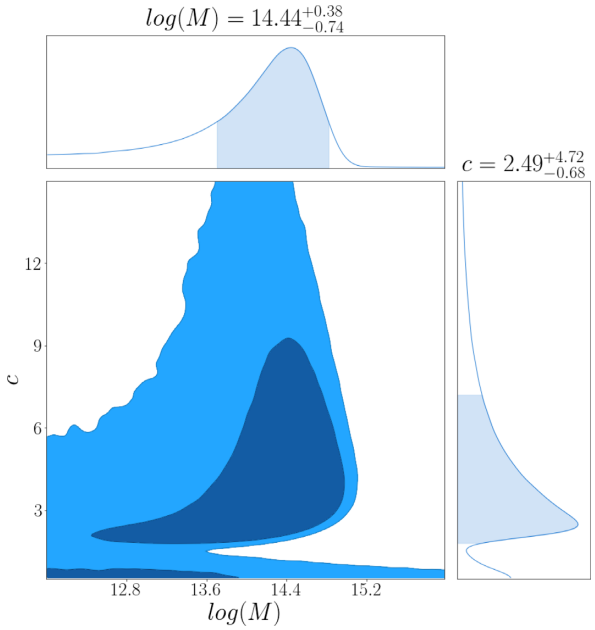

Figure 6. MCMC results for A 3560 with a pixel scale of 3 arcmin. The horizontal axis shows mass M_{200} in units of (h^{-1}M$_\odot$). The vertical axis shows concentration parameter. Contours are stepped by 1σ.

dispersion of 652 ± 84 km s^{-1}, based on 18 member galaxies within r_{200} (1.62 Mpc), where r_{200} was iteratively estimated from the σ_v as in Haines et al. (2018). This implies a mass $M_{200} = 5.7 \times 10^{14}$ M$_\odot$, comparable to that of Abell 3556.

The nature of the 5σ mass peak located at RA = 198.°8, Dec. = –33.°03 is less clear. It is located 20 arcmin south of the nearest cluster AS 0724 within the SSC, but also appears offset by 20 arcmin west from the extended structure at $z \sim 0.10$ that runs up the western boundary of the VST survey region (Chow-Martínez et al. 2014; Haines et al. 2018). The most likely correspondence appears to be with groups of galaxies at $z \sim 0.1$ to 0.3.

6.2 The $c-M$ relation of ShaSS massive clusters

Fig. 10 shows a comparison of the concentration parameters obtained from our fitting results and the $c-M$ relation derived by the simulations of Duffy et al. (2008). For the analytical model, the mean redshift of the clusters was adopted.

Although our results turn out to be consistent with the simulations within 2σ, the derived $c-M$ relations tend to be lower. While the results have large uncertainties, they could be explained by the dynamical state of the clusters. Previous studies showed that values of concentration parameters for unrelaxed clusters are lower than those for relaxed clusters of the same mass (Neto et al. 2007; Bhattacharya et al. 2013; Child et al. 2018; Okabe et al. 2019) and unrelaxed clusters having ∼ 30 per cent lower values of the concentration parameter in our mass range. Based on hierarchical structure formation, the high-overdensity environment of superclusters is more recently formed than normal clusters, so that the concentration of their components are expected to be lower. Therefore, the dynamical state or formation epoch of the constituent clusters could explain the smaller values of the concentration parameters in our results.

6.3 Cluster masses

In Fig. 11, we compared the WL-derived masses ($M_{\rm WL}$) with those derived from the dynamical analysis ($M_{\rm dyn}$) and listed in Table 1. The dynamical masses were computed under the assumption of the singular isothermal model and velocity dispersions (Haines et al. 2018). We obtained the WL masses for the four massive clusters (A 3556, A 3558, A 3560, and A 3562) with the MCMC method. On the other hand, we only gave the upper limit of the masses for six out of seven low-mass clusters due to the large shape noise in the WL analysis. In the figure, we labelled the low-mass clusters as black crosses, AS 0726 as black box and the four massive clusters as cyan circles. For AS 0726, we only indicatively adopted the average mass for the low-mass clusters derived using the stacked shear profile. We notice that (i) the masses obtained from the dynamical and WL analysis are consistent within 1σ for all clusters except A 3554,

Table 3. Fitting results of the massive clusters. The masses and concentration parameters are estimated by using the two-dimensional shear map with the pixel size of 3 arcmin. 1σ uncertainties are reported. Column (1): cluster name, Column (2): RA of BCG (°), Column (3): Dec. of BCG (°), Column (4): log [M_{200} (h^{-1}M$_\odot$)], and Column (5): concentration parameter.

Cluster name	RA	Dec.	M_{200} ($10^{14}h^{-1}M_\odot$)	c
A 3556	201.028071	−31.669883	$1.62^{+1.40}_{-1.08}$	$2.35^{+3.75}_{-0.47}$
A 3558	201.986930	−31.495891	$4.47^{+2.78}_{-2.38}$	$2.63^{+1.23}_{-0.55}$
A 3560	203.107375	−33.135833	$2.75^{+3.85}_{-2.25}$	$2.49^{+4.72}_{-0.68}$
A 3562	203.394788	−31.672261	$2.04^{+2.74}_{-1.78}$	

Table 4. Fitting results for the tangential shear profiles. Column (1): cluster name, Column (2): RA of BCG (°), Column (3): Dec. of BCG (°), Column (4): M_{200} (h^{-1}M$_\odot$), Column (5): concentration parameter, and Column (6): χ^2.

Cluster name	RA	Dec.	M_{200} ($10^{13}h^{-1}$M$_\odot$)	c	χ^2/dof
AS 0724	198.247 761	−33.002 6810	$2.34^{+8.09}$	$3.90^{+18.84}$	9.18/9
A 3552	199.729 591	−31.817 5762	$3.01^{+17.22}$	$3.73^{+24.51}$	14.33/9
A 3554	199.881 979	−33.488 1320	$4.29^{+6.49}$	$5.67^{+2.34}$	5.97/9
A 3559	202.462 143	−29.514 3931	$1.79^{+14.92}$	$3.55^{+27.45}$	8.38/9
SC 1327-312	202.367 236	−31.551 2698	$4.31^{+49.25}$	$2.39^{+4.66}$	11.21/9
SC 1329-313	202.864 741	−31.820 6321	$1.79^{+2.93}$	$6.35^{+21.76}$	3.12/9

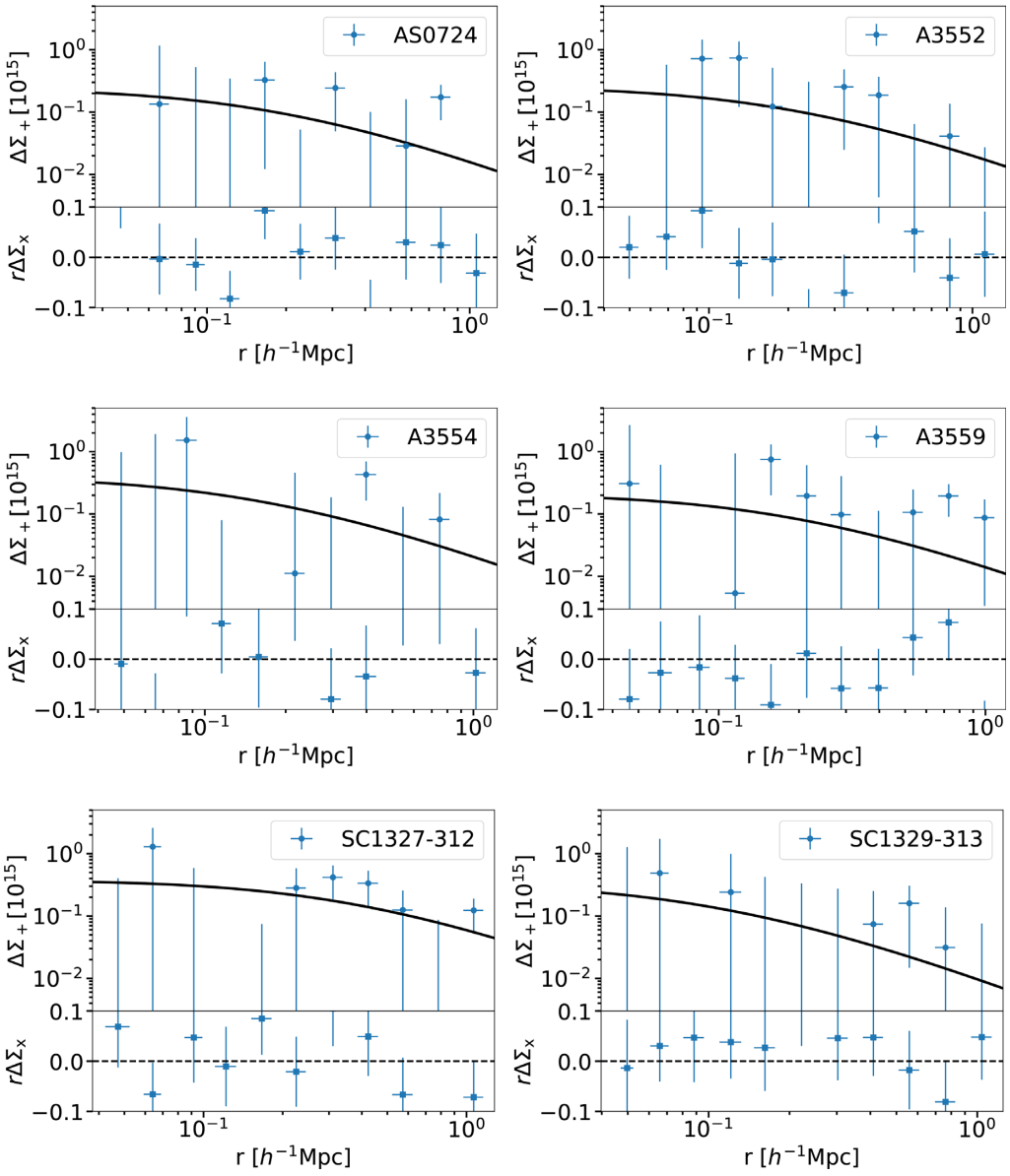

Figure 7. Tangential and cross-shear profiles for the low-mass clusters. The horizontal axis shows the distance from the BCG. The vertical axes for upper and lower panels show a tangential and cross shear profiles, respectively. The best-fitted NFW profiles are plotted as solid lines.

A 3558, and AS 0726; (ii) the dynamical masses turn out to be systematically higher than the WL-derived ones. Previous studies showed that WL masses obtained from the tangential shear fitting were biased low up to 10 per cent with a scatter of ∼25 per cent (Oguri et al. 2005; Sereno & Umetsu 2011; Sereno & Ettori 2015). The main source of the bias are due to substructures and triaxiality. When a cluster whose major axis is perpendicular to the line of sight, i.e elongated in the sky-plane, a mass obtained with the spherical NFW profile is typically underestimated. The presence of substructures around clusters and uncorrelated large-scale structures along the line of sight also generate the biases for the estimation of the WL masses (Meneghetti et al. 2010; Becker & Kravtsov 2011; Giocoli et al. 2012, 2014). In addition, we point out that the dynamical mass of AS 0726 is actually an upper limit since the velocity distribution of member galaxies is strongly bimodal, and certainly not Gaussian (see fig. 14 in Haines et al. 2018). This system probably consists of two groups with velocity dispersions ∼300 km s^{-1} rather than one single system with σ ∼600 km s^{-1}. This would reduce the mass estimate by a factor of 4. The complex structure of A 3558 and, in general, the dynamical activity in the SSC core (see Bardelli et al. 1998; Ettori et al. 2000; Finoguenov et al. 2004; Rossetti et al. 2007a) may explain the systematic differences between the two mass determinations quoted above, since the virial mass tends to overestimate the mass of unrelaxed clusters. Moreover, Rossetti et al. (2007b) studied A 3558 with an X-ray observation and showed the possibility of the presence of substructures along the line of sight, which interact with the cluster. Since such structures along the line of sight broaden velocity distribution, masses obtained from the dynamical analysis can be overestimated up to 100 per cent (Takizawa, Nagino & Matsushita 2010; Pratt et al. 2019). Fig. 14 in Haines et al. (2018) showed the broad velocity distribution of galaxies for the cluster. This indicates the presence of the substructures along the line of sight and the

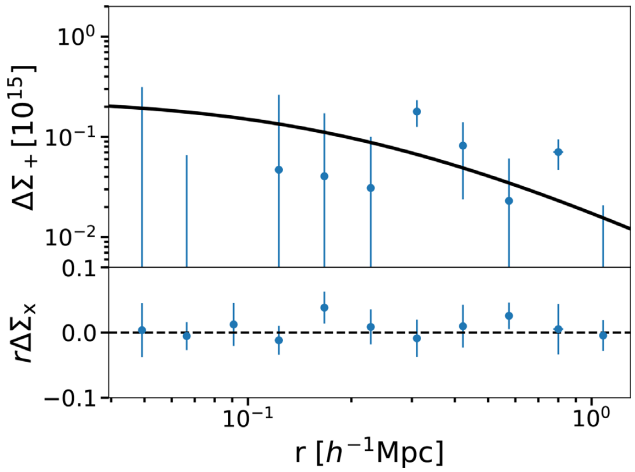

Figure 8. The stacked shear profile for the seven low-mass clusters. The horizontal axis shows the distance from the BCGs. The upper and lower panels show the tangential and cross shear, respectively. The points show the results obtained from the observation. The solid line shows the best-fitted result with the NFW profile.

possibility for overestimating the dynamical mass. A 3554 also shows strong substructures in the velocity distribution diagram.

The WL and dynamical mass estimates for the massive clusters are actually consistent within 1σ for three clusters and within 2σ for A3558, even though we used different measurement techniques and different mass models. Thus, the total mass of the four massive clusters does not dramatically differ between the two approaches. We found their total masses $\mathcal{M}_{\rm 4cl,dyn} = (3.42 \pm 0.20) \times 10^{15}{\rm M}_\odot$ and $\mathcal{M}_{\rm 4cl,WL} = (1.56^{+0.81}_{-0.55}) \times 10^{15}{\rm M}_\odot$ – i.e. only a factor of ∼2.2 lower. By using the empirical $L_{\rm X}$–M_{200} scaling relation of Böhringer, Chon & Collins (2014) (their equation 10), we obtain $\mathcal{M}_{\rm 4cl,X} = (2.23 \pm 0.7) \times 10^{15}{\rm M}_\odot$. The error of this estimates reflects the scatter of the mass–X-ray luminosity relation. While we could give upper limits of the masses for the low- mass clusters, we got the total mass for the 11 clusters $\mathcal{M}_{\rm ShaSS,WL} = (1.84^{+1.13}) \times 10^{15}{\rm M}_\odot$. In the calculation, we used the average mass derived from the stacking analysis for the mass of AS 0726. The total dynamical mass is $\mathcal{M}_{\rm ShaSS,dyn} = (4.80 \pm 2.3) \times 10^{15}{\rm M}_\odot$.

Quintana et al. (1995) estimated a mass for the whole SSC in the range 7×10^{15}–$7 \times 10^{16}\,{\rm M}_\odot$.[3] Ragone et al. (2006) identified 122 galaxy systems across a 12×15 deg^2 region centred in the SSC core and estimated their individual masses, which summed up result in a total mass of $\mathcal{M}_{\rm SSC} = 6.88 \times 10^{15}{\rm M}_\odot$. From the observed galaxy overdensity in a 285 deg^2 region, Proust et al. (2006) evaluated for the supercluster a total mass of $\mathcal{M}_{\rm SSC} = 7 \times 10^{16}{\rm M}_\odot$. They also claimed that the result of Ragone et al. (2006) is a lower limit for the SSC mass.

All these mass estimates referred to the whole supercluster, on the other hand, ShaSS covers 260 Mpc^2 centred on the core. Applying a spherical collapse model, Reisenegger et al. (2000) found that the SSC is gravitationally collapsing at least in its central region within a radius of $8\,h^{-1}$ Mpc, centred on A 3558 including 11 clusters; the very inner region, associated with the massive clusters, is likely in the final stages of collapse. The mass within this radius was found to be $\mathcal{M}_{\rm SSC} \sim 1.4 \times 10^{16}{\rm M}_\odot$. On the other end, they same authors using the heuristic escape-velocity methods of Diaferio & Geller (1997) obtained a mass estimate of $\mathcal{M}_{\rm SSC} \sim 2.9 \times 10^{15}{\rm M}_\odot$. This value is consistent within the errors with both our measurements of $\mathcal{M}_{\rm ShaSS,dyn}$ and $\mathcal{M}_{\rm ShaSS,WL}$.

[3]In the following, all the masses are converted into $H_0 = 70\,{\rm km\,s^{-1}\,Mpc^{-1}}$.

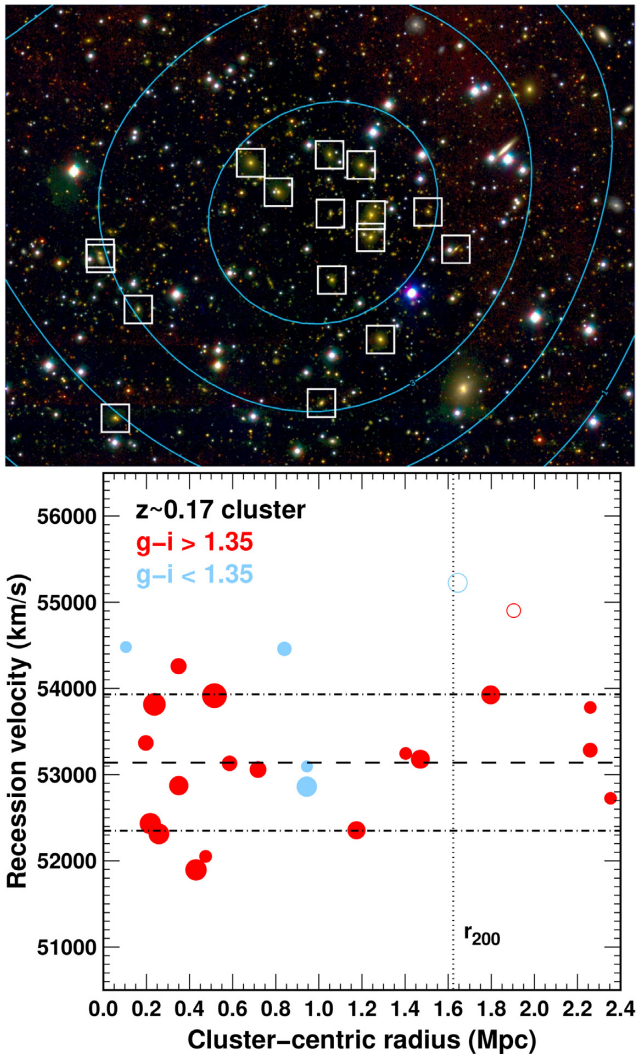

Figure 9. Upper panel: *gri* colour composite image centred on the WL detection (blue contours) of a background cluster at redshift $z \sim 0.17$. The blue contours indicate the WL peak. Lower panel: distribution of cluster members of the background cluster (solid dots, sizes scale with *i*-band luminosity) and non-members (open circles) in the caustic diagram; line-of-sight velocity,cz, versus projected distance from the centre of the WL peak. The dashed and dot–dashed lines indicate the central velocity and 1σ velocity dispersion of member galaxies within r_{200} (vertical dotted line).

7 SUMMARY AND CONCLUSIONS

With the aim to investigate the mass distribution and thus to trace the environment in the centre of the SSC (at $z \sim 0.048$), we have conducted the first WL analysis of a 260 Mpc^2 region around the supercluster core including 11 clusters. This study has taken advantage of the multiband (*gri*) optical imaging collected at European Southern Observatory–VST together with the related photometric catalogues. These data have allowed us to generate the galaxy shape catalogues in g and r bands across the whole surveyed region. In the following, the adopted approach is briefly described.

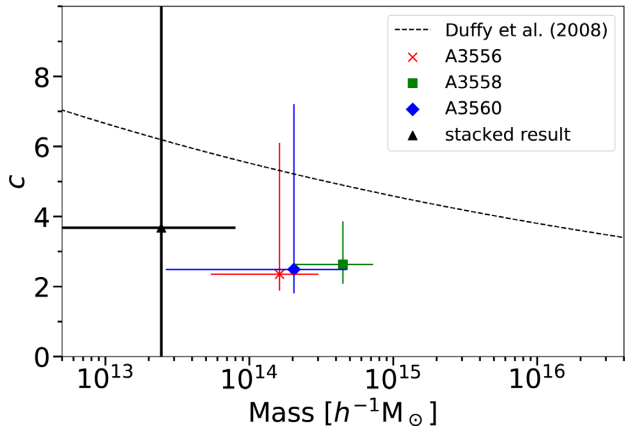

Figure 10. Comparison of $c-M$ relation between our result and the simulations of Duffy et al. (2008). The horizontal axis shows M_{200}. The vertical axis shows the concentration parameter. The dashed line shows the simulation result. The error bars show 1σ uncertainties.

(i) Supercluster members have been selected via photometric redshifts and background/foreground galaxies with the colour–colour diagram. The average density of the background galaxies turned out to be 7 arcmin^{-2}.

(ii) The project mass distributions, i.e. the WL mass maps have been derived for both *r*- and *g*-band data. The significance of the mass map has been estimated by randomizing the background galaxy shapes. The two maps allowed to double-check the final results especially in one fields affected by peculiar distortion.

(iii) Concentration parameters and masses were obtained fitting with the NFW profile the two-dimensional shear of the massive clusters (A 3556, A 3558, A 3560, and A 3562) and the tangential shear of the low-mass clusters (AS 0724, A 3552, A 3554, A 3559, SC 1327-312, and SC 1329-313). For the low-mass clusters, we have also fitted their stacked tangential shear profile estimating their average mass and concentration parameter.

Our analysis of the ShaSS provides further evidence of the complex structure of the system and cluster–cluster interactions, reveals a new background cluster of galaxies, and provides WL-derived masses for the 11 clusters embedded in a common network.

(i) We have found a tight correlation between WL mass distribution and the structure as traced by the galaxy density previously derived for the ShaSS. In particular, the WL map in *r* band highlights that the SSC core consists of a coherent system and shows indications of filaments connecting the SSC core and A 3559 in agreement with our previous study revealing a stream of galaxies in the same region.

(ii) The total WL-derived mass of the four massive clusters is $\mathcal{M}_{\rm ShaSS,WL} = (1.56^{+0.81}_{-0.55}) \times 10^{15}M_\odot$, which is consistent with their total dynamical mass. Adding the upper mass limits of the remaining clusters, the total mass is consistent with the total dynamical mass of Haines et al. (2018) and with Reisenegger et al. (2000), who analysed almost the same region of the ShaSS.

(iii) The WL-derived masses are found to be systematically lower than the dynamical ones for each cluster, although the different estimates are consistent within 1σ for eight out of ten clusters. This discrepancy can be explained by the fact that in such a perturbed and dynamically active environment, the cluster dynamical mass should be actually considered as an upper limit. In fact, the differences between the mass derivations are higher in the less relaxed and more substructured clusters. Likewise, the $c-M$ relation of ShaSS clusters shows concentration parameters typical of unrelaxed clusters.

(iv) Finally, in the WL mass map, we detect a peak associated to a previously unknown background cluster at $z \sim 0.177$ with a velocity dispersion of 652 ± 84 km s^{-1} (based on 18 member galaxies within $r_{200} = 1.62$ Mpc) and implying a mass $M_{200} = 5.7 \times 10^{14}$ M$_\odot$, comparable to that of A 3556.

We conclude that the WL and dynamical analyses are complementary and both essential for a robust characterization of the supercluster environment allowing us to ascertain the continuity of the SSC structure around the core and supporting the scenario of an ongoing collapse.

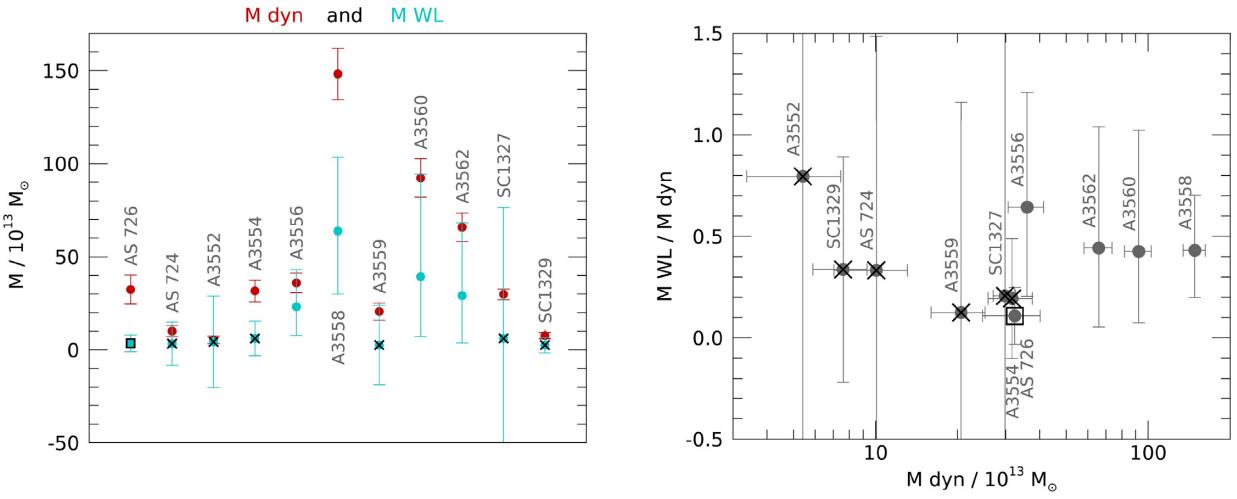

Figure 11. Left-hand panel: The WL-derived masses (M_{WL}, cyan circles) for the 11 clusters are compared with the with the dynamical masses (M_{dyn}, red circles). Black crosses denote the low-mass clusters (see Table 1). Open black square denotes AS0726 for which the average mass for the low-mass clusters is adopted. Right-hand panel: The ratio of WL-derived and dynamical masses as a function of the dynamical mass for the 11 clusters. The 1σ error bar is indicated in both panels.

ACKNOWLEDGEMENTS

We would like to thank the anonymous referee for giving useful comments and improving our manuscript. We would like to thank K.Umetsu, I.Chiu, and Y.Toba for useful comments and discussions. This work is supported by ALMA collaborative science research project 2018-07A, in part by the Ministry of Science and Technology of Taiwan (grant MOST 106-2628-M-001-003-MY3) and by Academia Sinica (grant AS-IA-107-M01). Numerical computations were in part carried out on Cray XC50 at Center for Computational Astrophysics, National Astronomical Observatory of Japan. Data analyses were (in part) carried out on common use data analysis computer system at the Astronomy Data Center, ADC, of the National Astronomical Observatory of Japan. The optical imaging is collected at the VST using the Italian INAF Guaranteed Time Observations. PM, GB and AM acknowledge financial support from INAF PRIN-SKA 2017 *ESKAPE* (PI L. Hunt).

DATA AVAILABILITY

The spectroscopic data underlying this paper are available at https://doi.org/10.1093/mnras/sty2338. The full multiband catalogue will be released in a forthcoming paper.

REFERENCES

Bardelli S., Pisani A., Ramella M., Zucca E., Zamorani G., 1998, MNRAS, 300, 589
Bardelli S., Zucca E., Zamorani G., Moscardini L., Scaramella R., 2000, MNRAS, 312, 540
Bartelmann M., Schneider P., 2001, Phys. Rep., 340, 291
Becker M. R., Kravtsov A. V., 2011, ApJ, 740, 25
Beers T. C., Flynn K., Gebhardt K., 1990, AJ, 100, 32
Bhattacharya S., Habib S., Heitmann K., Vikhlinin A., 2013, ApJ, 766, 32
Böhringer H., Chon G., Collins C. A., 2014, A&A, 570, A31
Bruzual G., Charlot S., 2003, MNRAS, 344, 1000
Bullock J. S., Kolatt T. S., Sigad Y., Somerville R. S., Kravtsov A. V., Klypin A. A., Primack J. R., Dekel A., 2001, MNRAS, 321, 559
Capaccioli M., Schipani P., 2011, The Messenger, 146, 2
Cava A. et al., 2009, A&A, 495, 707
Child H. L., Habib S., Heitmann K., Frontiere N., Finkel H., Pope A., Morozov V., 2018, ApJ, 859, 55
Chow-Martínez M., Andernach H., Caretta C. A., Trejo-Alonso J. J., 2014, MNRAS, 445, 4073
Courtois H. M., Tully R. B., Hoffman Y., Pomarède D., Graziani R., Dupuy A., 2017, ApJ, 847, L6
de Filippis E., Schindler S., Erben T., 2005, A&A, 444, 387
Diaferio A., Geller M. J., 1997, ApJ, 481, 633
Dietrich J. P., Werner N., Clowe D., Finoguenov A., Kitching T., Miller L., Simionescu A., 2012, Nature, 487, 202
Drinkwater M. J., Parker Q. A., Proust D., Slezak E., Quintana H., 2004, PASA, 21, 89
Duffy A. R., Schaye J., Kay S. T., Dalla Vecchia C., 2008, MNRAS, 390, L64
Einasto M. et al., 2016, A&A, 595, A70
Einasto M. et al., 2018, A&A, 620, A149
Einasto J., Hütsi G., Einasto M., Saar E., Tucker D. L., Müller V., Heinämäki P., Allam S. S., 2003, A&A, 405, 425
Einasto M., Liivamägi L. J., Tago E., Saar E., Tempel E., Einasto J., Martínez V. J., Heinämäki P., 2011, A&A, 532, A5
Einasto J., Suhhonenko I., Liivamägi L. J., Einasto M., 2019, A&A, 623, A97
Ettori S., Fabian A. C., White D. A., 1997, MNRAS, 289, 787
Ettori S., Bardelli S., de Grandi S., Molendi S., Zamorani G., Zucca E., 2000, MNRAS, 318, 239
Finoguenov A., Henriksen M. J., Briel U. G., de Plaa J., Kaastra J. S., 2004, ApJ, 611, 811
Galametz A. et al., 2018, MNRAS, 475, 4148
Giacintucci S. et al., 2005, A&A, 440, 867
Giocoli C., Meneghetti M., Ettori S., Moscardini L., 2012, MNRAS, 426, 1558
Giocoli C., Meneghetti M., Metcalf R. B., Ettori S., Moscardini L., 2014, MNRAS, 440, 1899
Gonzalez A. H., Zaritsky D., Zabludoff A. I., 2007, ApJ, 666, 147
Gonzalez A. H., Sivanandam S., Zabludoff A. I., Zaritsky D., 2013, ApJ, 778, 14
Grado A., Capaccioli M., Limatola L., Getman F., 2012, Mem. Soc. Astron. Ital. Suppl., 19, 362
Gray M. E. et al., 2009, MNRAS, 393, 1275
Haines C. P. et al., 2018, MNRAS, 481, 1055
Heymans C. et al., 2008, MNRAS, 385, 1431
Higuchi Y., Inoue K. T., 2019, MNRAS, 488, 5811
Higuchi Y., Oguri M., Shirasaki M., 2014, MNRAS, 441, 745
Hinton S. R., 2016, J. Open Source Softw., 1, 00045
Ilbert O. et al., 2013, A&A, 556, A55
Jee M. J., Hoekstra H., Mahdavi A., Babul A., 2014, ApJ, 783, 78
Jing Y. P., 2000, ApJ, 535, 30
Jones D. H. et al., 2009, MNRAS, 399, 683
Kaiser N., Squires G., 1993, ApJ, 404, 441
Kaiser N., Squires G., Broadhurst T., 1995, ApJ, 449, 460
Kaldare R., Colless M., Raychaudhury S., Peterson B. A., 2003, MNRAS, 339, 652
Kocevski D. D., Ebeling H., Mullis C. R., 2004, in Mulchaey J. S., Dressler A., Oemler A., eds, Clusters of Galaxies: Probes of Cosmological Structure and Galaxy Evolution, Carnegie observatories, California, p. 26
Kron R. G., 1980, ApJS, 43, 305
Kuijken K., 2011, The Messenger, 146, 8
Kull A., Böhringer H., 1999, A&A, 341, 23
Lubin L. M., Gal R. R., Lemaux B. C., Kocevski D. D., Squires G. K., 2009, AJ, 137, 4867
Mahajan S., Singh A., Shobhana D., 2018, MNRAS, 478, 4336
Maturi M., Merten J., 2013, A&A, 559, A112
Medezinski E., Broadhurst T., Umetsu K., Oguri M., Rephaeli Y., Benítez N., 2010, MNRAS, 405, 257
Mei S. et al., 2012, ApJ, 754, 141
Meneghetti M., Rasia E., Merten J., Bellagamba F., Ettori S., Mazzotta P., Dolag K., Marri S., 2010, A&A, 514, A93
Mercurio A. et al., 2015, MNRAS, 453, 3685
Merluzzi P. et al., 2015, MNRAS, 446, 803
Merluzzi P., Busarello G., Dopita M. A., Haines C. P., Steinhauser D., Bourdin H., Mazzotta P., 2016, MNRAS, 460, 3345
Miller N. A., 2005, AJ, 130, 2541
Muñoz J. A., Loeb A., 2008, MNRAS, 391, 1341
Navarro J. F., Frenk C. S., White S. D. M., 1997, ApJ, 490, 493
Neto A. F. et al., 2007, MNRAS, 381, 1450
Oguri M., Takahashi K., Ichiki K., Ohno H., 2004, preprint (astro-ph/0410145)
Oguri M., Takada M., Umetsu K., Broadhurst T., 2005, ApJ, 632, 841
Oguri M., Takada M., Okabe N., Smith G. P., 2010, MNRAS, 405, 2215
Oguri M., Bayliss M. B., Dahle H., Sharon K., Gladders M. D., Natarajan P., Hennawi J. F., Koester B. P., 2012, MNRAS, 420, 3213
Okabe N. et al., 2016, MNRAS, 456, 4475
Okabe N. et al., 2019, Publ. Astron. Soc. Japan, 71, 79
Okabe N., Umetsu K., 2008, PASJ, 60, 345
Okabe N., Takada M., Umetsu K., Futamase T., Smith G. P., 2010, PASJ, 62, 811
Okabe N., Smith G. P., Umetsu K., Takada M., Futamase T., 2013, ApJ, 769, L35
Okabe N., Futamase T., Kajisawa M., Kuroshima R., 2014, ApJ, 784, 90
Planck Collaboration et al., 2014, A&A, 571, A31
Pratt G. W., Arnaud M., Biviano A., Eckert D., Ettori S., Nagai D., Okabe N., Reiprich T. H., 2019, Space Sci. Rev., 215, 25
Proust D. et al., 2006, A&A, 447, 133
Quintana H., Ramirez A., Melnick J., Raychaudhury S., Slezak E., 1995, AJ, 110, 463

Quintana H., Melnick J., Proust D., Infante L., 1997, A&AS, 125, 247
Ragone C. J., Muriel H., Proust D., Reisenegger A., Quintana H., 2006, A&A, 445, 819
Raychaudhury S., 1989, Nature, 342, 251
Reisenegger A., Quintana H., Carrasco E. R., Maze J., 2000, AJ, 120, 523
Rossetti M., Ghizzardi S., Molendi S., Finoguenov A., 2007a, A&A, 463, 839
Rossetti M., Ghizzardi S., Molendi S., Finoguenov A., 2007b, A&A, 463, 839
Schlafly E. F., Finkbeiner D. P., 2011, ApJ, 737, 103
Sereno M., Ettori S., 2015, MNRAS, 450, 3633
Sereno M., Umetsu K., 2011, MNRAS, 416, 3187
Takizawa M., Nagino R., Matsushita K., 2010, PASJ, 62, 951
Tully R. B., 2005, ApJ, 618, 214
Umetsu K. et al., 2014, ApJ, 795, 163
Umetsu K., Medezinski E., Broadhurst T., Zitrin A., Okabe N., Hsieh B.-C., Molnar S. M., 2010, ApJ, 714, 1470
Umetsu K., Broadhurst T., Zitrin A., Medezinski E., Coe D., Postman M., 2011, ApJ, 738, 41
Umetsu K., Zitrin A., Gruen D., Merten J., Donahue M., Postman M., 2016, ApJ, 821, 116
Venturi T., Bardelli S., Dallacasa D., Brunetti G., Giacintucci S., Hunstead R. W., Morganti R., 2003, A&A, 402, 913
Wright C. O., Brainerd T. G., 2000, ApJ, 534, 34
Yaryura C. Y., Baugh C. M., Angulo R. E., 2011, MNRAS, 413, 1311
York D. G. et al., 2000, AJ, 120, 1579
Zhao D. H., Jing Y. P., Mo H. J., Börner G., 2009, ApJ, 707, 354

This paper has been typeset from a TEX/LATEX file prepared by the author.